HHS Public Access

Author manuscript

Biomaterials. Author manuscript; available in PMC 2022 January 01.

Published in final edited form as:

Biomaterials. 2021 January ; 265: 120411. doi:10.1016/j.biomaterials.2020.120411.

Lymph-directed nitric oxide increases immune cell access to lymph-borne nanoscale solutes

Lauren F. Sestito[1], **Susan N. Thomas**[1,2,3,4,*]

[1]Wallace H. Coulter School of Biomedical Engineering, Georgia Institute of Technology and Emory University, Atlanta, GA 30332

[2]Parker H. Petit Institute for Bioengineering and Bioscience, Georgia Institute of Technology, Atlanta, GA 30332

[3]George W. Woodruff School of Mechanical Engineering, Georgia Institute of Technology, Atlanta, GA 30332

[4]Winship Cancer Institute, Emory University, Atlanta, GA 30332

Abstract

Lymph nodes (LNs) are immune organs housing high concentrations of lymphocytes, making them critical targets for therapeutic immunomodulation in a wide variety of diseases. While there is great interest in targeted drug delivery to LNs, many nanoscale drug delivery carriers have limited access to parenchymal resident immune cells compared to small molecules, limiting their efficacy. Nitric oxide (NO) is a potent regulator of vascular and lymphatic transport and a promising candidate for modulating nanocarrier access to LNs, but its lymphatic accumulation is limited by its low molecular weight and high reactivity. In this work, we employ S-nitrosated nanoparticles (SNO-NP), a lymphatic-targeted delivery system for controlled NO release, to investigate the effect of NO application on molecule accumulation and distribution within the LN. We evaluated the LN accumulation, spatial distribution, and cellular distribution of a panel of fluorescent tracers after intradermal administration alongside SNO-NP or a small molecule NO donor. While SNO-NP did not alter total tracer accumulation in draining lymph nodes (dLNs) or affect active cellular transport of large molecules from the injection site, its application enhanced the penetration of nanoscale 30 nm dextrans into the LN and their subsequent uptake by LN-

*To whom correspondence should be addressed: Susan N. Thomas, Ph.D., Georgia Institute of Technology, IBB 2310, 315 Ferst Drive NW, Atlanta, GA 30332, 404-385-1126, susan.thomas@gatech.edu.

CRediT Author Statement

Lauren F. Sestito: Conceptualization, methodology, formal analysis, investigation, writing – original draft, writing – review and editing, visualization

Susan N. Thomas: Conceptualization, methodology, writing – review and editing, supervision, project administration, funding acquisition

DATA AVAILABILITY STATEMENT

The data that support the findings of this study are available from the corresponding author upon reasonable request.

Declaration of interests

The authors declare that they have no known competing financial interests or personal relationships that could have appeared to influence the work reported in this paper.

resident lymphocytes, while nontargeted NO delivery did not. These results further extended to a peptide-conjugated NP drug delivery system, which showed enhanced uptake by B cells and dendritic cells when administered alongside SNO-NP. Together, these results highlight the utility of LN-targeted NO application for the enhancement of nanocarrier access to therapeutically relevant LN-resident immune cells, making NO a potentially useful tool for improving LN drug delivery and immune responses.

Keywords

nitric oxide; nanoparticle; lymph node; lymphatic system; transport

INTRODUCTION

Lymph nodes (LNs) are complex secondary lymphoid organs consisting of high concentrations of lymphocytes supported by stromal cells, extracellular matrix (ECM), and blood and lymphatic vessels [1]. Because of their critical role in the immune response, LNs are valuable therapeutic targets for immune modulation in a variety of contexts, including infectious disease vaccination [2,3], tolerance induction [4,5], cancer immunization [6], and prevention of graft rejection [7,8]. Therapeutics delivered for these purposes are diverse, and include small molecule drugs, peptides, larger antigen, combination nanoparticle (NP) delivery vehicles, and even microparticles, covering a broad range of molecule sizes. Regardless of the disease context, in order for LN-targeted delivery to be useful, these diverse therapeutics must be able to reach the lymphatics at sufficiently high concentrations, and have access to target cells within the LN. Therapeutic delivery to LN-resident cells is complicated, however, by biological barriers that inhibit drug accumulation in LNs and subsequent access to LN-localized immune cells.

The most direct route of molecule access to LNs is via their afferent lymphatics, taking advantage of lymph drainage patterns that shuttle interstitial fluid and its soluble factors from peripheral tissue directly to LNs. This pathway is critical in the immune response, providing rapid transport of migratory immune cells, antigen, and cytokines to waiting LN-resident lymphocytes, and can also be exploited for targeted drug delivery to LNs. In the clinic, peripheral injection into intradermal (i.d.) or subcutaneous spaces is commonly employed for a wide variety of drugs, including monoclonal antibody (mAb) adalimumab (Humira) and fusion protein etanercept (Enbrel) for the management of autoimmune diseases; common vaccines including varicella, Bacillus Calmette–Guérin, and measles, mumps, and rubella vaccines; allergen immunotherapies; and even cancer treatments, including chemotherapeutic bortezomib and mAb rituximab. Improving LN access of such peripherally administered drugs is thus an active area of research. Vaccine efficacy has been shown to be improved by antigen or adjuvant conjugation to nanoscale carriers that promote lymphatic drainage [3,9], and similarly improved outcomes are observed when NPs are used to promote co-delivery of antigen and tolerogenic agents to LNs for the treatment of autoimmune disease [5,10]. These benefits have also been observed in cancer vaccination and immunotherapy, where increased delivery of tumor antigen and adjuvants to LN

improves the anti-tumor immune response [6,11]. Enhancing LN access of peripherally administered drugs thus has significant clinical implications in a variety of disease contexts.

In the context of lymphatic transport regulation, nitric oxide (NO) is of particular interest. This reactive small molecule is known for its inflammatory action and vasoactive effects within the blood vasculature, but it is also a critical regulator of lymphatic pumping, vascular permeability, and immune cell activation, all of which can regulate transport within the lymphatics (Fig. 1A). Local application of NO could impact drug partitioning into blood and lymph from the interstitial space due to NO's enhancement of vascular permeability [12–14], and NO has been observed to alter the activation and migration of skin-resident migratory dendritic cells (DCs) [15]. NO is also a critical regulator of lymphatic vessel contractility [16–18], giving it the potential to modulate transport of lymph-draining molecules and their rate of accumulation within LN. Within the LN, NO regulates many pathways that could alter intra-LN molecular transport and subsequent cellular uptake. For example, NO reduces the integrity of lymphatic endothelial cell (LEC) cell-cell junctions, enhancing the permeability of the lymphatic endothelium [12,19]; increases blood vascular permeability and remodels LN vasculature [20]; and critically regulates immune cell activation and proliferation [21]. Because of its many roles within the lymphatics, NO could be a promising tool with which to regulate drug access to lymphatics and lymph node-resident cells.

While NO has been applied therapeutically for the treatment of angina [22] and pulmonary hypertension [23], its short half-life and low molecular weight make targeted NO delivery to lymphatic tissues challenging. To overcome these limitations and enable concentrated NO delivery to LNs, we previously developed S-nitrosated nanoparticles (SNO-NP) and characterized their NO release and delivery both *in vitro* [24] and *in vivo* [25]. SNO-NP were shown to release NO in the form of nitrite over the course of days [24,25], and to be capable of transnitrosation of biological small molecule thiols [24]. When administered *in vivo*, SNO-NP significantly improved accumulation of NO in LN compared to a traditional small molecule NO donor [25]. Herein, we apply this LN-targeted, NO donation system to investigate the effect of NO on lymphatic transport and LN distribution of co-delivered molecules, modeled using a panel of fluorescent tracers over a biologically relevant size range. We demonstrate that while SNO-NP application did not alter active transport of large molecules from the site of injection, passive lymph drainage, or total LN accumulation of small- or medium-sized molecules, NO delivery to LN significantly increased the penetration of typically excluded mid-size (30 nm) molecules into the LN and enhanced their subsequent uptake by cortical B cells and paracortical T cells. Increased access to parenchymal LN cells was observed in both model dextran molecules and an antigen-conjugated NP drug delivery system, highlighting the versatility of NO's effects. LN-targeted NO application thus represents a promising tool for the enhancement of drug delivery vehicle access to parenchymal LN-resident cells to facilitate improved control of the immune response.

MATERIALS AND METHODS

Materials

All materials were purchased from Sigma Aldrich unless otherwise noted.

NP synthesis and characterization

SH-NP were synthesized as previously described [25]. Briefly, 500 mg of Pluronic F127 was added to 10 mL of MilliQ water under argon and dissolved by stirring at 1500 rpm. 400 μl of propylene sulfide (TCI, Tokyo, Japan) was then added under argon. After 30 min, 42 mg of thiolated initiator (synthesized as previously described [26]) that had been activated in 322 μl of sodium methoxide for 15 min was added under argon, and the mixture was stirred for 15 min. 64 μl of 1,8-diazabicyclo[5.4.0] undec-7-ene was added under argon, and the solution was capped. After 24 h, the reaction was exposed to air for 2 h to cross-link the NP poly(propylene sulfide) core, and the NP were then dialyzed in a 100,000 Da membrane (Spectrum Labs, New Brunswick, NJ) against 5 L of Milli-Q water for three d, with six water changes. NP size was measured by dynamic light scattering on a Malvern ZetaSizer instrument. In select experiments, NP were reacted overnight at room temperature with an excess of Alexa Fluor 647 C_2 maleimide (Thermo Fisher, Waltham, MA) and cleaned of unreacted dye by size exclusion chromatograpy. SH-NP were nitrosated immediately before use by the addition of sodium nitrite in 0.5M hydrochloric acid. Excess sodium nitrite was quenched by addition of ammonium sulfamate, and SNO-NP were cleaned using a 7kDa Zeba column (Thermo Fisher). To evaluate NO release from SNO-NP, SNO-NP in 1X PBS were incubated in a closed tube at 37°C, and SNO and NO_2 concentrations were monitored over time using the Saville and Griess assays, respectively. To characterize NP drainage to and accumulation in draining LN from a forelimb injection, Alexa Fluor 647-labeled NP were injected i.d. in the forelimbs of mice. 24 h after injection, animals were sacrificed and skin removed to expose axillary and brachial LNs. Exposed LN were imaged using fluorescence detection on an IVIS Spectrum CT instrument, and fluorescent signal was quantified using LivingImage software. LN fluorescence levels were compared to animals injected in the forelimbs with either saline or unconjugated Alexa Fluor 647-NHS ester of equivalent brightness inactivated by overnight incubation at room temperature.

NP-S-S-CSIINFEKL were synthesized from pyridyl disulfide-functionalized NP (PDS-NP). PDS-NP were synthesized as previously described [27]. First, carboxylate-Pluronic F127 was synthesized. Briefly, 23.6 g of Pluronic F127 was dissolved in 500 mL of toluene. To this solution, 2.6 mL of triethylamine and 1.4 mL of methanesulfonyl chloride were added and reacted for 18 h. The solution was filtered, concentrated under reduced pressure, and precipitated in ether. The resulting solid was dissolved in 100 mL of dimethylformamide (DMF), and 2.29 g of potassium carbonate and 2 mL of mercaptopropionic acid methyl ester was added. After 20 h, the solution was concentrated under vacuum, dissolved in 100 mL DCM, and cleaned with 8 g of activated carbon. The carbon was removed by filtration, and the remaining solution was concentrated and precipitated in ether. The resulting Pluronic thioether propionic acid methyl ester was dissolved in 200 mL of Milli-Q water, reacted overnight with 0.57 g of sodium hydroxide, dialyzed for three days against 5 L of Milli-Q water, and lyophilized to yield carboxylate-Pluronic F127. COOH-NP were synthesized as

described previously using carboxylate-Pluronic F127 rather than Pluronic F127. NP were labeled by reaction in 1X PBS with Alexa Fluor 647 C_2 maleimide (Thermo Fisher) overnight, and remaining unreacted core thiols were capped by reaction with N-ethylmaleimide (NEM) until no thiol signal could be detected by the Ellman's assay. NP were PDS functionalized by consecutive reaction with EDC, NHS, and PDS in MES buffer overnight, followed by dialysis for three days. NP-S-S-CSIINFEKL were produced by reacting CSIINFEKL peptide (New England Peptide) with PDS-NP overnight, and NP-S-S-CSIINFEKL were cleaned of unreacted peptide by size exclusion chromatography using a CL-6B resin and concentrated for use.

Fluorescent tracers

Red and yellow-green carboxylate-modified 0.5 μm FluoSpheres were purchased from Thermo Fisher. 10 kDa and 500 kDa amine-dextrans were labeled by reaction in PBS with Alexa Fluor 610 *N*-hydroxysuccinimide (NHS) ester (Thermo Fisher) or Alexa Fluor 647 NHS ester (Thermo Fisher), respectively. Alternatively, 10 kDa Alexa Fluor 647-labeled dextran (Thermo Fisher) and 500 kDa tetramethylrhodamine isothiocyanate (TRITC)-labeled dextran (Sigma-Aldrich, St. Louis, MO) were purchased. Tracers labeled with a fluorophore in-house were purified of unreacted free dye by size exclusion chromatography using a CL-6B resin and concentrated before use. Tracer size was verified by DLS (Supp. Fig. 1A, B). All tracers were maintained under sterile conditions.

Biodistribution experiments

Mice were simultaneously administered both NO treatment or controls and a tracer cocktail as a single injection into the forelimb skin. Treatment groups included SNO-NP delivering 800 nmol NO, as measured by the Saville assay; dose-matched SH-NP; S-nitroso-N-acetylpenicillamine (SNAP) delivering 800 nmol of NO; or saline. The tracer cocktail included red FluoSpheres (500 nm), Alexa Fluor 647 500 kDa dextran (30 nm), and Alexa Fluor 610 10 kDa dextran (5 nm) at 1.2×10^8 spheres, 23.8 μg, and 3 μg, respectively. All components were delivered in a single 40 μl injection. At 4, 24, or 72 h after injection, animals were sacrificed and blood was harvested by cardiac puncture. Other organs, including liver, kidney, spleen, and LNs draining the forelimb injection (axillary + brachial, pooled) were harvested, weighed, and homogenized in 400 μl of 1X PBS using 1.4mm acid washed zirconium beads (OPS Diagnostics, Lebanon, NJ). The fluorescence of 100 μl of each tissue homogenate was measured in triplicate using a Synergy H4 BioTek plate reader. After compensation was applied to account for the low overlap in tracer fluorescence, the concentration of each tracer in each tissue was calculated using standard curves generated in a background of each individual tissue homogenate. Tracer concentrations below the limit of detection in each tissue were considered undetectable (Supp. Fig. 1C).

In experiments to evaluate tracer access to LNs from the circulation, fur was removed from the dorsal skin of mice and treatment (700 nmol SNO-NP, dose-matched SH-NP, 700 nmol SNAP, or saline) was injected i.d. in four locations in the dorsal skin: above the left and right shoulders and the left and right flanks. Four mice were used per treatment (in two independent experiments), and each mouse received four injections of the same treatment. Immediately, animals were given a tracer cocktail containing 238 μg Alexa Fluor 647 500

kDa dextran (30 nm), 58.6 μg Alexa Fluor 700 40 kDa dextran (10 nm), and 30 μg Alexa Fluor 610 10 kDa dextran (5 nm) by intravenous injection in the jugular vein. 4 h after tracer injection, animals were sacrificed and axillary, brachial, and inguinal LN draining the dorsal injections were individually harvested, homogenized, and their fluorescence analyzed as previously described.

Lymph node immune cell uptake experiments

In *in vivo* tracer uptake experiments, mice received 40 μl injections in both forelimbs containing both a tracer cocktail and NO treatment or controls. Treatment groups included SNO-NP delivering 800 nmol NO, as measured by the Saville assay; dose-matched SH-NP; SNAP delivering 800 nmol of NO; or saline. The tracer cocktail included yellow-green FluoSpheres (500 nm), TRITC 500 kDa dextran (30 nm), and Alexa Fluor 647 10 kDa dextran (5 nm) at 1.2×10^8 spheres, 23.8 μg, and 3 μg, respectively. A sample size of three mice with two forelimb injections each was used for each treatment group, and the full experiment was repeated twice. 72 h after injection, when all NO is expected to be released, animals were sacrificed and LNs draining the forelimb injection (axillary and brachial) were harvested. After 30 min incubation with 1 mg/ml collagenase D at 37°C, LN were gently separated through a 70 μm cell strainer using a 1 mL syringe plunger, and the strainer was thoroughly washed. Cells were isolated by centrifugation at 400 rcf for 5 min, and pellets were resuspended and transferred to a round bottom 96 well plate for staining. Cells were incubated with 100 μl of 2.5 μg/ml 2.4G2 (Tonbo Biosciences, San Diego, CA) for 5 min on ice, followed by incubation with Zombie Aqua Live/Dead (Biolegend, San Diego, CA) for 30 min at room temperature. Cells were then incubated with a cocktail of antibodies in FACS buffer (1% bovine serum albumin in 1X PBS) for 30 min on ice: PerCP CD45, PE/Cy7 DEC205, APC/Cy7 CD11b, BV421 CD11c, BV605 CD169, BV650 B220, BV711 CD3, and BV785 F4/80. All antibodies were purchased from Biolegend. After antibody staining, cells were fixed by incubation with 2% paraformaldehyde (PFA) for 15 min on ice, thoroughly washed, and resuspended in FACS buffer for analysis. Data was acquired using an LSRFortessa flow cytometer (BD Biosciences, Franklin Lakes, NJ), and analyzed using FlowJo software (FlowJo, Ashland, OR). Cell types were defined as follows: B cells: B220+CD3-CD11b-; T cells: CD3+B220-; conventional dendritic cells (cDCs): CD11c +B220-; plasmacytoid dendritic cells (pDCs): CD11c+B220+; subcapsular sinus macrophages (SSMs):B220-CD3-CD11b+CD11c+CD169+F4/80-; medullary sinus macrophages (MSMs): B220-CD3-CD11b+CD11c+CD169+F4/80+; medullary cord macrophages (MCMs): B220-CD3-CD11b+CD11c+CD169-F4/80+; dermal dendritic cells (dDCs): $CD11c^{hi}$DEC205+; and Langerhans cells (LCs): $CD11c^{lo}$DEC205+. Within each cell type, tracer+ populations were identified by comparison to tracer- cells from LN draining a saline injection (Supp. Fig. 2).

For *in vivo* NP-S-S-CSIINFEKL uptake experiments, NO treatment (800 nmol SNO-NP, SH-NP, or saline) was injected i.d. in mouse forelimbs. Alexa Fluor 647-labeled NP-S-S-CSIINFEKL were simultaneously injected alongside NO treatment in a single, 40 μl injection. Animals were sacrificed 72 h after NO treatment injection, and axillary and brachial LN were harvested and separated through a 70 μm cell strainer. Cells were stained with Zombie Aqua Live/Dead and an antibody cocktail (PerCP CD45, PE H-$2K^b$ bound to

SIINFEKL, APC/Cy7 CD11b, BV421 CD11c, BV605 CD169, FITC B220, BV711 CD3, and BV785 F4/80, all purchased from Biolegend) and fixed by 15 min exposure to 2% PFA as described above before analysis by flow cytometry.

Confocal imaging

To evaluate typical LN distribution of 5, 30, and 500 nm tracers, 40μl of saline containing 1.2×10^8 yellow-green FluoSpheres (500 nm), 23.8 μg TRITC 500 kDa dextran (30 nm), and 3 μg Alexa Fluor 647 10 kDa dextran (5 nm) was injected i.d. in the forelimbs of mice. 72 h after injection, animals were sacrificed, and axillary and brachial LN were individually frozen in OCT. LNs were sliced into 10 μm sections using a CryoStar NX70 Cryostat, mounted on slides, and imaged in all three tracer channels using a laser scanning confocal microscope (Zeiss 700 scanning head on an AxioObserver Z1 inverted microscope stage). Using ImageJ software (NIH), the capsule of each LN was individually traced, and the coordinates exported using a custom ImageJ macro. Images were thresholded to remove background, with thresholding values for each tracer determined using a control LN with no tracer injection. After thresholding, the coordinates of the remaining tracer+ pixels were extracted, and the minimum distance of each pixel from the LN capsule was calculated using a custom MATLAB script.

For evaluation of the effect of SNO-NP treatment on tracer LN distribution, mice were given i.d. forelimb injections containing both NO treatment (SNO-NP delivering 800 nmol NO, dose-matched SNAP, dose-matched SH-NP, or saline) and tracer cocktail (yellow-green FluoSpheres (500 nm), TRITC 500 kDa dextran (30 nm), and Alexa Fluor 647 10 kDa dextran (5 nm) at 1.2×10^8 spheres, 23.8 μg, and 3 μg, respectively). Three mice were injected in each NO treatment group and axillary and brachial LN were separately imaged, yielding six images per treatment. After 72 h, axillary and brachial LN draining the forelimb injection were extracted, cleaned, and imaged in all three tracer channels using a laser scanning confocal microscope (Zeiss 700 scanning head on an AxioObserver Z1 inverted microscope stage). Z-stacks were taken centered around the brightest plane in each LN. Using Zen software (Zeiss), z-stacks were converted to maximum intensity projections and images separated into individual tracer channels. Using ImageJ software (NIH), the capsule of each LN was individually traced, and the coordinates exported using a custom ImageJ macro. Images were thresholded to remove background, with thresholding values for each tracer determined using a control LN with no tracer injection. After thresholding, the coordinates of the remaining tracer+ pixels were extracted, and the minimum distance of each pixel from the LN capsule was calculated using a custom MATLAB script.

In vitro dextran uptake and junction staining

For splenocyte uptake experiments, splenocytes were isolated from the spleens of C57/Bl6 mice. Spleens were gently separated and pushed through a 70 μm cell strainer using a syringe plunger to generate a single cell suspension. Red blood cells were lysed by 5 min incubation with 1 mL of ACK Lysing Buffer (Thermo Fisher), followed by dilution in 40 mL of 1X PBS and centrifugation to isolate splenocytes. Splenocytes were counted, and 1 million cells were plated in each well of a 96 well, U-bottom plate with 200ul of RPMI 1640 medium. To this cell suspension was added NO treatment (SNO-NP at 0.16 mM NO, dose-

matched SH-NP, SNAP at 0.16 mM NO, or saline), followed immediately by a tracer cocktail (Alexa Fluor 647-labeled 10 kDa dextran, TRITC-labeled 500 kDa dextran, and 500 nm yellow-green spheres). After incubation for 4 h at 37°C, splenocytes were stained and fixed for flow cytometric analysis as previously described. Stains included Zombie Aqua Live/Dead, PerCP CD45, APC/Cy7 CD11b, BV421 CD11c, BV650 B220, and BV711 CD3.

For LEC uptake experiments, SV-LECs [28] (kindly provided by Dr. J. Brandon Dixon) were seeded at 90% confluency in collagen-coated 24-well plates and allowed to adhere for 24 h. 400 μl of EBM containing 1 mg/ml TRITC-labeled 500 kDa dextran was added to each well alongside NO treatment (SNO-NP at 0.16mM NO, dose-matched SH-NP, SNAP at 0.16 mM NO, or saline). After 4 h of incubation at 37°C, LECs were washed with 1X PBS to remove remaining dextran, and the adherent cells were imaged using the RFP channel on an EVOS microscope. LECs that had not been incubated with dextran were imaged to obtain a background, and wells with dextran but without LECs were imaged to verify that washing successfully removed all extracellular dextran. After imaging, cells were detached from their plates by brief incubation with 0.25% trypsin and were transferred to U-bottom 96 well plates. The fluorescence of the cell suspensions in 100 μl of PBS were measured using a Synergy H4 BioTek plate reader, and cells were subsequently stained for flow cytometric analysis with Zombie Aqua Live/Dead and PerCP CD31 (Biolegend) as previously described.

To investigate LEC expression of tight junction protein zonula occludens-1 (ZO-1), SV-LECs were grown to confluency in collagen-coated 96-well plates or 8-well Lab-Tek chamber slides (Thermo Fisher) and allowed at least 48 h to form junctions. LECs were treated with SNO-NP at 0.16 mM NO, dose-matched SH-NP, or saline for 6 h. Cells were detached from 96-well plates via trypsin treatment and prepared for flow cytometric analysis. Briefly, cells were incubated with 2.4G2 for 5 min on ice, stained with Zombie Red Live/Dead (Biolegend), fixed in 4% PFA for 10 min at room temperature, permeabilized with 0.1% Triton-X for 10 min at room temperature, and stained with ZO-1 primary antibody (Thermo Fisher) or rabbit IgG isotype control and Alexa Fluor 488-conjugated anti-rabbit IgG secondary (Thermo Fisher) for 1 h each. Samples were analyzed on an LSR II flow cytometer (BD). For confocal imaging, adherent cells were fixed in 4% PFA, permeabilized with 0.1% Triton-X, and blocked with 1% bovine serum albumin. They were incubated at 4°C overnight with ZO-1 primary antibody or isotype, then stained with secondary antibody for 1 h at room temperature. Slides were mounted in DAPI-containing Vectashield and imaged using a laser scanning confocal microscope.

LEC monolayer transport

5×10^4 SV-LECs (P34–36) were seeded in 6.5 mm, 0.4 μm polyester transwell inserts (Corning) and allowed 48 h to settle, adhere, and form monolayers. 1 mg/ml Alexa Fluor 610-labeled 10 kDa dextran (5 nm) and 1 mg/ml TRITC-labeled 500 kDa dextran (30 nm) were added to the EBM medium in the transwell insert alongside treatment with 0.16mM SNO-NP, SH-NP, or PBS. At 0, 1, 3, 5, 8, 24, and 48 h, media from the bottom chamber of the transwell was sampled, and the presence of both 10 kDa and 500 kDa dextran was evaluated by measuring media fluorescence using a Synergy H4 BioTek plate reader. After

48 h, LECs were detached from the membranes by trypsin treatment, stained with Zombie Aqua Live/Dead, and their viability analyzed by flow cytometry.

Statistical Analysis

All data are presented as mean ± standard error of the mean, and statistical analyses were performed in Prism 8 (GraphPad Software Inc., La Jolla, CA). Statistical significance was defined as $p < 0.05$ following an unpaired t-test or ordinary one-way analysis of variance with Tukey posthoc testing as appropriate. Symbols denoting p-values are as follows: * = $p < 0.05$, ** = $p < 0.01$, *** = $p < 0.001$, and **** = $p < 0.0001$.

Animal Use

All animal procedures were performed at Georgia Institute of Technology, and were approved by the Georgia Institute of Technology Institutional Animal Care and Use Committee. All mice were female C57BL6/J, and were used at 6–10 weeks of age.

RESULTS

NO delivery to draining LNs via SNO-NP

We have previously reported the generation of S-nitrosated nanoparticles (SNO-NP) capable of extended NO donation in both *in vitro* [24] and *in vivo* [25] applications. These SNO-NP are based on a polymeric nanoparticle which consists of a Pluronic corona and a hydrophobic poly(propylene sulfide) core containing large numbers of free thiols [24]. These thiolated NP (SH-NP) can be quickly loaded with NO by addition of nitrite under acidic conditions, converting thiols into *S*-nitrosothiols (SNO) [24,25] (Fig. 1A). SNO-NP provide extended NO donation, as evidenced by the gradual decrease in SNO concentration and appearance of nitrite (NO_2) when SNO-NP were incubated at 37°C for several days [24,25] (Fig. 1B). While i.d. injection of unconjugated, small molecule (~1300 Da) Alexa Fluor 647 in the mouse forelimb did not increase the fluorescent signal in axillary and brachial LN draining the injection above background, Alexa Fluor 647-labeled NP injection resulted in clear dye accumulation in these LN (Fig. 1C, D), highlighting the lymphatic uptake and LN access advantage provided by NP compared to small molecule injection [25,29]. Because of the importance of size in the advantageous lymph drainage properties of these NP, NP diameter was measured by dynamic light scattering before and after NO loading (Fig. 1E). Treatment with acidified nitrite did not affect the hydrodynamic radius or the polydispersity of the NP, suggesting that their critical size and stability is retained after *S*-nitrosation of the core thiols. This is consistent with previous studies, in which we have observed that intradermal injection of SNO-NP results in significant accumulation of SNO in draining LN 72 h after injection [25]. Together, the lymph-draining size of these NP and the extended NO release that they provide make SNO-NP a unique tool for lymphatic-targeted NO delivery and the investigation of NO's role in biomolecule transport.

Fluorescent tracer characterization

To interrogate the effect of NO application on the biodistribution of co-injected molecules, we developed a panel of fluorescent tracers to probe the distinct pathways of size-based lymphatic transport (Fig. 2A). 5 nm tracer represents small molecules that are primarily

absorbed into the bloodstream [29,30], but which have access to the deep LN parenchyma via the conduit system upon reaching the LN [31–33]. Mid-size molecules, represented by 30 nm tracers, show preferential lymphatic uptake, but are unable to access LN conduits, and large molecules that cannot passively drain into lymph and instead rely on active transport by migratory APCs are modeled by 500 nm tracers [34,35]. These three tracer sizes were modeled by 10 kDa dextran, 500 kDa dextran, and 500 nm polystyrene spheres, respectively; tracer hydrodynamic diameters were verified by dynamic light scattering (Fig. 2B). After an i.d. injection, these tracers distributed in systemic tissues in accordance with their size; 5 nm tracers were primarily cleared by the kidney and 30 nm by the liver, while 500 nm spheres reliant on active cellular transport were undetected in systemic tissues even 72 h after injection (Fig. 2C).

Tracers also differentially accumulated in LNs draining a forelimb injection in accordance with their size, as measured by monitoring fluorescent signal in LN homogenate (Fig. 2D). 30 nm tracers showed highest levels of LN accumulation, with levels remaining consistent from 4–72 h. 5 and 500 nm tracers accumulated to lower extents, as is expected due to the reduced lymphatic access of 5 nm tracers and the slow, active transport of 500 nm tracers. Notably, 500 nm tracers showed minimal accumulation at early time points and peak signal at 72 h, consistent with the time required for peripheral APCs to transport the spheres to the LN. To evaluate not only bulk accumulation of tracer in the LN, but also their spatial distribution, axillary and brachial LNs were imaged by confocal microscopy 72 h after forelimb injection of the tracer cocktail (Fig. 2E-G). 5 and 30 nm tracers, soluble molecules which enter the LN in afferent lymph via the sinuses, expectedly appeared in peripheral LN regions. 30 nm tracers, however, showed a stronger bias towards the LN periphery; the number of 30 nm+ pixels rapidly declined with increasing penetration depth compared to the smaller 5 nm tracer (Fig. 2F), resulting in a subtly reduced average penetration depth (Fig. 2G). 500 nm spheres appeared deep within the LN due to their transport within migratory DCs (Fig. 2E), and showed increased presence in these most central LN regions (Fig. 2F) and increased average penetration depth (Fig. 2G) compared to passively transported tracers. Along with distinct spatial distributions, tracers showed cellular distributions consistent with their size. Passively draining 5 and 30 nm tracers associated preferentially with CD11c+ DCs and F4/80+ macrophages, but 5 nm tracers had improved access to all cell types, including B cells in the cortex and T cells in the paracortex (Fig. 2H). 500 nm spheres showed significantly increased presence in CD11c+ DCs compared to other cell types (Fig. 2I), consistent with their reliance on active transport from the periphery. Together, the tracers employed probe distinct lymphatic transport pathways in both the interstitium and the LN, and enable studies of the effect of NO on molecule access to therapeutically relevant LN regions.

SNO-NP modulation of active cell transport of large particles

NO is a potent immune modulator, and exogenous NO application has been shown to induce migration of mature DCs [15]. To investigate the effect of SNO-NP on local immune cell activation and trafficking, we administered a tracer cocktail of 5, 30, and 500 nm fluorescent tracers in the mouse forelimb alongside SNO-NP treatment or controls. At 4, 24, and 72 h post-injection, dLN were dissected and either homogenized for the measurement of bulk

tracer accumulation, or analyzed by flow cytometry to evaluate cellular distribution of the tracer within the LN (Fig. 3A). The total amount of 500 nm tracer that reached the dLN was unaltered 72 h after injection by SNO-NP treatment (Fig. 3B), and the total LN exposure (AUC) was similarly unaffected (Fig. 3C). As an additional control, another group of mice was given SNAP, a 220 Da *S*-nitrosothiol NO donor with a similar NO release profile to SNO-NP. Because it is a small molecule, SNAP drains inefficiently to LN from an i.d. injection and does not result in significant NO delivery to lymphatic tissues [25], and thus provides a control for NO effects at the site of injection. SNAP treatment also had no effect on 500 nm accumulation compared to the saline vehicle, indicating that strictly local NO donation also did not modulate the overall amount of tracer trafficked. To investigate the cellular distribution of 500 nm tracer within the dLN, LN cells were further analyzed by flow cytometry. While 500 nm tracer uptake by CD45+ cells was clearly detectable within the LNs, neither SNO-NP nor SNAP treatment changed the frequency of these cells that were 500 nm+ compared to vehicle controls (Fig. 3D, E). NO treatment also did not affect the number of migratory cells, specifically dermal DCs (dDCs) and Langerhan's cells (LCs), positive for 500 nm tracer within dLNs (Fig. 3F), suggesting that NO application did not cause increased migration of local DCs to the dLN. While 500 nm signal was observed in a wide variety of cell types, including cortical B cells, paracortex T cells, conventional DCs (cDCs), plasmacytoid DCs (pDCs), migratory dDCs and LCs, and barrier subcapsular sinus macrophages (SSMs) (Fig. 3G), in no cell type was the frequency of cells 500 nm+ (Fig. 3H) or the 500 nm mean fluorescent intensity (MFI) (Fig. 3I) impacted by treatment with SNO-NP or SNAP. The unchanged number, frequency, and MFI of 500 nm+ migratory cells suggest that in this context, NO injection does not impact the migration of skin-resident APCs (#, %) or their ability to take up 500 nm tracer (MFI), nor does it impact overall 500 nm access to LN-resident cell populations. Together, these data indicate that SNO-NP can be administered i.d. without significantly altering migration or behavior of skin-resident APCs, consistent with previous observations that SNO-NP injection in the skin does not cause local inflammation [25].

LN distribution of lymph draining tracers with NO treatment

We next investigated the accumulation and distribution of passively transported 5 and 30 nm tracers in LNs draining a forelimb injection. 72 h after co-injection of tracers and SNO-NP or controls, at which point complete NO release from SNO-NP is expected, confocal imaging of axillary and brachial LNs revealed a typical distribution; both 5 and 30 nm tracers appeared most concentrated in peripheral LN regions, consistent with their passive drainage via afferent lymph (Fig. 4A, Supp. Fig. 3). In saline, SNAP, and SH-NP control treatments, 5 nm tracer appears to penetrate deeper into the LN than 30 nm tracer, consistent with its smaller size. In SNO-NP-treated LNs, however, this difference in penetration depth was not visibly clear. When the distance of each tracer+ pixel from the LN capsule was quantified, we observed that while saline, SNAP, and SH-NP injections all showed a similar trend of 30 nm tracers penetrating less deeply into LNs relative to less restricted 5 nm tracers, as evidenced by the curves' negative slopes, SNO-NP treatment prevented this decline and increased the LN penetration depth of 30 nm tracers (Fig. 4B). These effects were not observed with SNAP treatment, highlighting the importance of NO delivery to the LN. As NO is a known regulator of vascular permeability [12–14], we verified that NO

administration did not alter tracer clearance into circulation and resulting systemic distribution of tracer (Supp. Fig. 4A) or the kinetics of tracer appearance in systemic organs (Supp. Fig. 4B). We also investigated the effect of SNO-NP application on the access of circulating tracers to LNs (Supp. Fig. 4C-D). LNs treated with NO showed no change in accumulation of intravenously administered tracers, suggesting that SNO-NP do not change tracer access to LNs from the LN blood vasculature. Because of NO's known role in regulating contractility and function of lymphatic vessels, we investigated the effect of NO treatment on passive tracer accumulation within the LN, and found that the amount of both 5 and 30 nm tracer in dLNs was unchanged by treatment at any measured time point, and the total LN exposure to tracer (AUC) was similarly unaffected (Fig. 4C). Together, these results suggest that the increased LN penetration of 30 nm tracer was not observed due to altered tracer accumulation in the LN.

To further investigate the potential mechanism for the increased 30 nm penetration observed *in vivo*, transport of 30 nm dextran was studied *in vitro* using cultured SV-LECs (Supp. Fig. 5, Supp. Fig. 6A, B). When SV-LECs were incubated with fluorescent 30 nm tracer, SNO-NP-treated cells appeared to have increased tracer uptake compared to SH-NP controls (Fig. 4D). This enhanced uptake was also reflected in total fluorescence measured using a plate reader, where SNO-NP increased 30 nm uptake by SV-LECs compared to vehicle control (Fig. 4E) Flow cytometric analysis of the LECs showed an increase in their tracer MFI, but no change in the percent of cells tracer+ (Supp. Fig. 6C), suggesting that increased fluorescence measured via a plate reader was due to an increase in the amount of 30 nm tracer each LEC contained. While SNO-NP treatment did appear to increase 30 nm tracer uptake by LECs (Fig. 4D, E), it did not alter their distribution or expression of tight junction protein zonula occludens-1 (ZO-1); the percent of LECs expressing ZO-1 (Supp. Fig. 6D) and their MFI (Supp. Fig. 6E) were unchanged by SNO-NP treatment, and confocal microscopy showed no clear alterations in junction structure (Supp. Fig. 6F). Tracer transport across a LEC barrier was further investigated using a monolayer of SV-LECs cultured on the apical side of a transwell membrane insert. When fluorescent 5 and 30 nm tracers were added to the apical medium, tracer signal in the basal medium 48 h later was significantly reduced by the presence of a LEC monolayer compared to a cell-free membrane (Fig. 4F). While 5 nm signal was reduced only 3-fold, 30 nm signal was reduced by approximately 30-fold, consistent with a higher permeability of the LEC monolayer to 5 nm tracer than to 30 nm tracer. When LEC monolayers were treated additionally with SNO-NP or SH-NP and tracer transport across the monolayer was monitored over time, there was no difference in 5 nm signal at any time point, or in the nonlinear fit of the two curves (Fig. 4G). In contrast, 30 nm transport across the monolayer was increased by SNO-NP treatment, resulting in a significantly different curve fit compared to SH-NP control (Fig. 4G). This altered transport was not due to changes in LEC viability, which was consistent across treatment groups (Fig. 4H).

In addition to the spatial distribution of tracer, the cellular distribution of tracer within dLN was evaluated by flow cytometry. Treatment with SNO-NP did not affect LN size or cellularity compared to SH-NP control; total CD45+ cell counts (Fig. 5A) and LN cellular composition (Fig. 5B) remained consistent with treatment. Passively draining 5 and 30 nm tracers were clearly detectable in these CD45+ populations (Fig. 5C). While 5 nm uptake

was unchanged by SNO-NP treatment, the percent of CD45+ cells that were 30 nm+ significantly increased with SNO-NP treatment compared to the SH-NP vehicle control (Fig. 5C, D). This increased uptake was not observed with SNAP treatment. Much of the increased 30 nm uptake could be attributed to B cells and T cells; both cell types showed increased numbers of 30 nm+ cells with SNO-NP treatment compared to SH-NP control (Fig. 5E), and an increase in the percent of B cells that contained 30 nm tracer was also observed (Fig. 5F). SNO-NP did not increase 30 nm+ cell counts or frequencies in cDCs, pDCs, or SSMs, and small molecule NO donor SNAP had no effect on tracer uptake by either metric in any cell type (Fig. 5E, F). SNO-NP not only increased the number of 30 nm + B and T cells, but also increased the MFI of those 30 nm+ cells compared to vehicle control (Fig. 5G). A nonsignificant increase in 30 nm+ MFI was also observed in pDCs, centrally located cells within the LN. Overall, SNO-NP induced no alterations in 30 nm uptake within peripherally located SSMs, but cortical B cells showed significant increases in number, percent, and MFI of 30nm+ cells, and paracortical T cells had increased number and MFI (Fig. 5H). This enhanced 30 nm association was not accompanied by increased 5 nm signal; the frequency of cells positive (Fig. 5I) and their MFI (Fig. 5J) was unchanged by either SNO-NP or SNAP treatment.

To investigate if SNO-NP treatment had direct effects on 30 nm tracer uptake by immune cells, murine splenocytes were incubated with 30 nm tracer and SNO-NP or SH-NP *in vitro*. When splenocytes were analyzed by flow cytometry after 4 h, SNO-NP did not increase 30 nm tracer uptake by B cell, T cells, cDCs, or pDCs compared to SH-NP (Fig. 5K), further suggesting that the increased 30 nm uptake observed *in vivo* was not due to direct effects of NO on endocytosis by these immune cells.

NO effects on NP access and antigen presentation within the LN

With evidence that SNO-NP treatment can increase access of 30 nm dextran to LN resident cells, we next sought to extend these studies to other lymph-draining molecules and evaluate SNO-NP's effects on immune cell function *in vivo*. To this end, the model peptide antigen SIINFEKL was conjugated to the corona of an Alexa Fluor 647-labeled, PDS-functionalized NP via a cysteine added to the peptide's N-terminus, yielding NP-S-S-CSIINFEKL trackable by Alexa Fluor 647 fluorescent signal (Fig. 6A, Supp. Fig. 7A). When splenocytes were incubated with increasing doses of NP-S-S-CSIINFEKL *in vitro* and antigen presentation was evaluated by staining with an antibody recognizing H-2K^{b} bound to SIINFEKL, increasing CSIINFEKL presentation was detected with increasing delivered dose as measured by cell count (Fig. 6B) and MFI (Fig. 6C), suggesting that neither delivery via a NP vehicle nor the addition of a cysteine to SIINFEKL's N-terminus prevent presentation of the antigen. 72 h after injection in the forelimb, NP-S-S-CSIINFEKL positivity was clearly detectable in CD45+ cells within the dLN based on Alexa Fluor 647 signal (Fig. 6D). When NP-S-S-CSIINFEKL were co-administered with SNO-NP or control SH-NP, SNO-NP significantly increased the fraction of both B cells and cDCs that were Alexa Fluor 647+, and nonsignificantly increased the fraction of Alexa Fluor 647+ T cells and pDCs (Fig. 6E). In B cells, the Alexa Fluor 647 MFI also increased (Fig. 6F), suggesting that each Alexa Fluor 647+ cell contained more NP. The fraction and MFI of Alexa Fluor 647+ T cells and pDCs were insignificantly increased (Fig. 6E-F), an observation consistent

with the lowly phagocytic nature of these paracortex-resident cells. Cells were additionally stained for SIINFEKL presentation, revealing a NP+CSIINFEKL+ population in the dLN that both contained NP-S-S-CSIINFEKL and presented the delivered antigen (Fig. 6G). In B cells, cDCs, and pDCs that would be expected to present the antigen (Supp. Fig. 7C), SNO-NP treatment did not alter the frequency of cells that were NP+CSIINFEKL+ (Fig. 6H), nor did it alter the MFI of those CSIINFEKL-presenting cells (Fig. 6I). In addition to showing no increase in antigen presentation in spite of the enhanced NP uptake observed, neither B cells, pDCs, nor cDCs showed changes in the frequency (Fig. 6J) or intensity (Fig. 6K) of CD40 expression, expected to increase on mature APCs including B cells [36]. Together, these results suggest that the uptake enhancement afforded by SNO-NP is not attributed to alteration of APC activation, and is applicable not only to flexible dextrans, but also to a nanocarrier drug delivery system.

DISCUSSION

LNs are therapeutic tissue targets of great clinical significance; because of the high concentration of lymphocytes resident in these immune organs, drug delivery to lymphatic tissues represents a promising strategy for immunomodulation and management of a wide variety of applications, including infectious disease, autoimmune disease, and cancer. The lymphatic-targeting advantages provided by peripheral injection are well-established, and peripheral injection is accordingly employed in the clinic to promote lymphatic delivery and improve patient compliance. Nanoscale drug delivery vehicles are often applied to enable delivery of smaller drugs that would otherwise have poor lymphatic uptake due to their small size. While delivering drug via a nanoscale carrier improves lymphatic uptake of the drug from the interstitium, the larger size of the carrier may paradoxically reduce its ability to penetrate into parenchymal regions of the LN, limiting drug access to resident lymphocytes. Accordingly, a system that enables timed drug release from nanocarriers within LN has been shown to improve lymphocyte uptake of the delivered drug and subsequently improve therapeutic efficacy [37]. Improving LN penetration and lymphocyte access of the nanocarrier itself could have similar advantages.

In this study, we investigated the effect of NO on lymphatic transport and LN access of peripherally administered molecules, as NO is a well-established regulator of lymphatic transport in a wide variety of contexts (Fig. 1A). Using SNO-NP, which are polymeric nanoparticles that enable lymphatic uptake and LN accumulation of small molecule NO [25] (Fig. 1C, D), and a panel of model fluorescent tracers over a biologically relevant size range (Fig. 2B), we quantified LN accumulation, penetration, and cellular distribution of small, nanoscale, and microscale molecules after treatment with LN-targeted NO. We observed that although SNO-NP treatment did not affect systemic drainage (Supp. Fig. 4A, B) or LN accumulation (Fig. 4C) of passively transported 30 nm dextrans, their uptake by cortical B cells and paracortical T cells was enhanced by SNO-NP injection (Fig. 5E-G). This effect was particularly stark in B cells, in which the number, frequency, and MFI of tracer+ cells were all increased. T cells showed an increase in the number of tracer+ cells as well as MFI, but the frequency of T cells positive for tracer was unchanged by treatment, potentially owing to their less phagocytic nature. While only subtle effects of SNO-NP treatment were observed in cDCs and pDCs, which also reside in the paracortex, this could potentially be

attributed to the comparatively high baseline 30 nm uptake by these cell types (Fig. 5F). The enhanced tracer presence in B cells did not appear to be due to direct effects of NO on tracer uptake by immune cells, as uptake of co-administered 5 nm dextran was unaltered (Fig. 5I, J), and treatment with SNO-NP *in vitro* did not increase tracer uptake (Fig. 5K). Confocal microscopy revealed that with SNO-NP treatment, 30 nm dextran penetration into the LN was enhanced relative to mobile 5 nm dextran (Fig. 4A, B). *In vitro,* SNO-NP treatment also increased the permeability of a LEC monolayer to 30 nm dextran compared to treatment with control SH-NP (Fig. 4G), suggesting that NO delivery by SNO-NP may improve 30 nm dextran uptake by resident lymphocytes by increasing its ability to penetrate the LN. Though the exact mechanism of this increased permeability is unknown, *in vitro* treatment of SV-LECs with SNO-NP resulted in increased uptake of 30 nm tracers (Fig. 4E). As LECs are known to have vesicular, transcytotic transport pathways that result in shuttling of molecules like antibodies [38] and dextrans [39] across a LEC barrier, this enhanced uptake could potentially suggest an increase in transcytotic transport. Additionally, NO is a known regulator of blood and lymphatic vascular permeability through its effects on cell junction proteins [12–14,40]. While SNO-NP treatment did not appear to affect LEC expression of tight junction protein ZO-1 *in vitro* (Supp. Fig. 6 D-F), other junction proteins can be investigated in future work to fully evaluate the role of junctional disruption in the observed permeability increase. The increased cellular uptake observed in 30 nm dextran appeared to extend to peptide-loaded NP-S-S-CSIINFEKL, which after i.d. injection with SNO-NP showed enhanced uptake by B cells and cDCs, and subtly increased association with T cells and pDCs (Fig. 6E, F). This enhanced association occurred without visible effects of delivered NO on cell activation, as SIINFEKL presentation and CD40 expression by LN-resident antigen-presenting cells were unaltered by SNO-NP injection (Fig. 6H-K).

While SNO-NP administration increased LN penetration and lymphocyte uptake of co-delivered 30 nm dextran, administration of SNAP, a small molecule NO donor, had no such effects; SNAP did not result in enhanced tracer uptake by LN-resident cells (Fig. 5D-F), nor did it improve tracer penetration into the LN compared to a saline-treated control (Fig. 4B). Due to its size, SNAP is cleared rapidly from the peripheral injection site into circulation. While some low rate of drainage into lymph may be expected, akin to the drainage observed in 5 nm dextrans (Fig. 2D), administration of even a high concentration of SNAP does not result in detectable SNO presence in dLN [25]. SNAP is analogous to other small molecule NO formulations currently employed in the clinic and in research, including NO donors such as S-nitrosoglutathione [13], NONOates [14,19,41], glyceryl trinitrate [17,22,42], and sodium nitroprusside[19], which due to their size have poor lymphatic access and a short half-life in circulation. SNO-NP, employed here and previously described [24,25], represent a unique tool to overcome the limitations of conventional NO donors. Their efficacy compared to SNAP suggests that LN-targeted NO delivery is critical to elicit transport changes in this context, and highlights the value of the lymphatic-draining SNO-NP system.

While NO has previously been challenging to apply in the context of the lymphatics because of its small size and high reactivity, studying the role of NO in lymphatic transport is also complicated by the multifaceted effects NO can exert. It is perhaps one of the most prolific endogenous signaling molecules, and plays dose- and context-dependent roles in vascular and lymphatic permeability [12–14,19], vasodilation [43], coagulation [44,45], immune cell

activation and proliferation [21], and lymphatic contractility [16,17], among many other pathways. While its versatility means that NO has the potential to improve molecular transport to and within the LN in a way that could benefit drug access and efficacy, it could also inhibit such transport. For example, both endogenous [16] and exogenous [17] NO has been shown to inhibit lymphatic vessel contractions *in vivo* and impair normal lymph transport. When we investigated the effect of SNO-NP and SNAP injection on the accumulation of passively draining dextrans, however, we found that neither NO donor reduced the accumulation of dextran in dLN at 4, 24, or 72 h after injection compared to controls (Fig. 4C). This consistent tracer accumulation regardless of NO application allows the comparison of tracer spatial and cellular distribution within the LN between groups, but it should be noted that this observation does not preclude the presence of inhibited lymphatic pumping *in vivo* with SNO-NP administration, which we have not directly evaluated; tracer accumulation in dLN may just be sufficiently high that it is not reduced, in this context, by impaired lymph transport. Because of NO's role as an inflammatory signaling molecule and evidence that its application can alter the viability and migration of skin-resident APCs [15,46], we additionally evaluated the effect of NO on active transport of microparticles from the forelimb to dLN within migratory dDCs and LCs. Perhaps surprisingly, NO application did not alter the number of migratory DCs that carried tracer to the LN (Fig. 3F), regardless of its formulation. This is consistent with previous studies that showed i.d. administration of SNO-NP did not induce local inflammation [25] and supports the application of SNO-NP for LN-targeted NO delivery without injection site morbidity, and additionally highlights the importance of context and concentration of NO delivery.

In this work, we investigated the effect of LN-targeted NO delivery on LN access and distribution of both a 30 nm dextran tracer and a 30 nm peptide-conjugated polymer NP. Although similar in hydrodynamic diameter, these molecules are structurally distinct; model dextran is a more flexible molecule with a higher aspect ratio, while NP-S-S-CSIINFEKL are particulate in nature. In spite of their differences, both dextran and peptide-conjugated NPs showed enhanced uptake in B cells, as measured by both frequency and MFI of positive cells, with SNO-NP treatment. While dextran additionally showed increased MFI in paracortex T cells (Fig. 5G), this effect was only subtly observed in peptide-NP (Fig. 6C). Peptide-conjugated NP were also found in a higher frequency of cDCs with SNO-NP administration, an effect that was not observed in the flexible dextran, and both dextran and peptide-NP showed only nonsignificantly enhanced uptake in pDCs, as measured by MFI. These subtle differences in distribution between dextran and NP may be attributed to the variability in their size and structure, which is known to impact lymphatic transport [47], and its impact on cellular uptake, and differences in uptake between cell types may be a function of both their location within the LN and their inherent phagocytic properties. B cells and cDCs, for example, are more peripherally located compared to T cells and pDCs in the paracortex, which may contribute to the increased frequency of B cells and cDCs positive for dextran or peptide-NP. More subtle effects on MFI were observed in T cells and pDCs, which are both more centrally located and less inherently phagocytic than B cells and cDCs. While the dextran and polymer NP investigated are not fully representative of the diverse drug delivery vehicles employed for LN drug delivery, observing similar effects of NO on LN cellular distribution in two similarly-sized but structurally distinct molecules is a

promising start. Future work could expand NO application to other vehicles employed for lymphatic drug delivery, including metallic NP [48], liposomes [3], or silica NP [11], or investigate the upper size limit of NO's enhanced uptake effects.

CONCLUSIONS

In summary, we have employed a SNO-NP system to deliver NO specifically to lymphatic tissues as a tool to investigate the effect of LN-targeted NO on the lymphatic transport of co-delivered molecules over a biologically relevant size range. By monitoring the LN accumulation, distribution, and cellular uptake of 5, 30, and 500 nm tracers, we demonstrated that when delivered to the LN in a controlled, sustained fashion, NO can improve the penetration of nanoscale molecules into the LN and subsequently increase their uptake by parenchymal lymphocytes 72 h after i.d. injection. Model 30 nm dextrans showed increased association with B cells and T cells with SNO-NP administration, without alteration in total tracer accumulation in the LN or significant effects on migratory immune cell trafficking from the site of injection. The effects of SNO-NP were further extended to a peptide-conjugated NP, which showed increased uptake particularly by B cells and cDCs *in vivo*. As peripheral administration is the optimal route for lymphatic targeting and also commonly used in the clinic, enhancing the access of passively transported, lymph-draining molecules, including nanoscale drug delivery vehicles, to immune cells deep within the LN parenchyma has the potential to improving drug delivery to these therapeutically important cells and improve immunomodulatory treatments.

Supplementary Material

Refer to Web version on PubMed Central for supplementary material.

ACKNOWLEDGEMENTS

This work was supported by US National Institutes of Health grants R01CA207619, R01CA247484, U01CA214354, and T32EB006343 (LFS). LFS was an American Heart Association Pre-doctoral Fellow.

REFERENCES

[1]. Willard-Mack CL, Normal Structure, Function, and Histology of Lymph Nodes, Toxicol. Pathol 34 (2006) 409–424. 10.1080/01926230600867727. [PubMed: 17067937]

[2]. St John AL, Chan CY, Staats HF, Leong KW, Abraham SN, Synthetic mast-cell granules as adjuvants to promote and polarize immunity in lymph nodes., Nat. Mater 11 (2012) 250–7. 10.1038/nmat3222. [PubMed: 22266469]

[3]. Moon JJ, Suh H, V Li A, Ockenhouse CF, Yadava A, Irvine DJ, Enhancing humoral responses to a malaria antigen with nanoparticle vaccines that expand Tfh cells and promote germinal center induction., Proc. Natl. Acad. Sci. U. S. A 109 (2012) 1080–5. 10.1073/pnas.1112648109. [PubMed: 22247289]

[4]. Tostanoski LH, Chiu Y-C, Gammon JM, Simon T, Andorko JI, Bromberg JS, Jewell CM, Reprogramming the Local Lymph Node Microenvironment Promotes Tolerance that Is Systemic and Antigen Specific., Cell Rep. 16 (2016) 2940–2952. 10.1016/j.celrep.2016.08.033. [PubMed: 27626664]

[5]. Maldonado RA, LaMothe RA, Ferrari JD, Zhang AH, Rossi RJ, Kolte PN, Griset AP, O'Neil C, Altreuter DH, Browning E, Johnston L, Farokhzad OC, Langer R, Scott DW, Von Andrian UH, Kishimoto TK, Polymeric synthetic nanoparticles for the induction of antigen-specific

immunological tolerance, Proc. Natl. Acad. Sci. U. S. A 112 (2015) E156–E165. 10.1073/pnas.1408686111. [PubMed: 25548186]

[6]. Thomas SN, Vokali E, Lund AW, Hubbell JA, Swartz MA, Targeting the tumor-draining lymph node with adjuvanted nanoparticles reshapes the anti-tumor immune response, Biomaterials. 35 (2014) 814–824. 10.1016/J.BIOMATERIALS.2013.10.003. [PubMed: 24144906]

[7]. Bahmani B, Uehara M, Jiang L, Ordikhani F, Banouni N, Ichimura T, Solhjou Z, Furtmüller GJ, Brandacher G, Alvarez D, von Andrian UH, Uchimura K, Xu Q, Vohra I, Yilmam OA, Haik Y, Azzi J, Kasinath V, Bromberg JS, McGrath MM, Abdi R, Targeted delivery of immune therapeutics to lymph nodes prolongs cardiac allograft survival, J. Clin. Invest 128 (2018) 4770–4786. 10.1172/JCI120923. [PubMed: 30277476]

[8]. Plšková J, Holán V, Filipec M, V Forrester J, Lymph node removal enhances corneal graft survival in mice at high risk of rejection, 2004. http://www.biomedcentral.com/1471-2415/4/3 (accessed May 5, 2020).

[9]. Liu H, Moynihan KD, Zheng Y, Szeto GL, V Li A, Huang B, Van Egeren DS, Park C, Irvine DJ, Structure-based Programming of Lymph Node Targeting in Molecular Vaccines, Nature. 507 (2014) 519–522. 10.1038/nature12978. [PubMed: 24531764]

[10]. Capini C, Jaturanpinyo M, Chang H-I, Mutalik S, McNally A, Street S, Steptoe R, O'Sullivan B, Davies N, Thomas R, Antigen-specific suppression of inflammatory arthritis using liposomes., J. Immunol 182 (2009) 3556–65. 10.4049/jimmunol.0802972. [PubMed: 19265134]

[11]. An M, Li M, Xi J, Liu H, Silica Nanoparticle as a Lymph Node Targeting Platform for Vaccine Delivery, ACS Appl. Mater. Interfaces 9 (2017) 23466–23475. 10.1021/acsami.7b06024. [PubMed: 28640587]

[12]. Durán WN, V Beuve A, Sánchez FA, Nitric oxide S-nitrosation, and endothelial permeability., IUBMB Life. 65 (2013) 819–26. 10.1002/iub.1204. [PubMed: 24078390]

[13]. Thibeault S, Rautureau Y, Oubaha M, Faubert D, Wilkes BC, Delisle C, Gratton J-P, S-Nitrosylation of Beta-Catenin by eNOS-Derived NO Promotes VEGF-Induced Endothelial Cell Permeability, Mol. Cell (2010) 468–476. https://reader.elsevier.com/reader/sd/pii/S1097276510005356?token=E4F13A6968D16FD50FA33006C45C86EB716115C56ABFE21915B1F7F3213001B472970D873876CB1FD43D21D10F41AA5E (accessed April 27, 2020). [PubMed: 20705246]

[14]. Yang B, Cai B, Deng P, Wu X, Guan Y, Zhang B, Cai W, Schaper J, Schaper W, Nitric oxide increases arterial endotheial permeability through mediating VE-cadherin expression during arteriogenesis, PLoS One. 10 (2015) e0127931. 10.1371/journal.pone.0127931.

[15]. Giordano D, Magaletti DM, Clark EA, Nitric oxide and cGMP protein kinase (cGK) regulate dendritic-cell migration toward the lymph-node-directing chemokine CCL19, Blood. 107 (2006) 1537–1545. 10.1182/blood-2005-07-2901. [PubMed: 16249377]

[16]. Liao S, Cheng G, Conner DA, Huang Y, Kucherlapati RS, Munn LL, Ruddle NH, Jain RK, Fukumura D, Padera TP, Impaired lymphatic contraction associated with immunosuppression., Proc. Natl. Acad. Sci. U. S. A 108 (2011) 18784–9. 10.1073/pnas.1116152108. [PubMed: 22065738]

[17]. Weiler M, Kassis T, Dixon JB, Sensitivity analysis of near-infrared functional lymphatic imaging., J. Biomed. Opt 17 (2012) 066019. 10.1117/1.JBO.17.6.066019.

[18]. Bohlen HG, Gasheva OY, Zawieja DC, Nitric oxide formation by lymphatic bulb and valves is a major regulatory component of lymphatic pumping., Am. J. Physiol. Heart Circ. Physiol 301 (2011) H1897–906. 10.1152/ajpheart.00260.2011. [PubMed: 21890688]

[19]. Scallan JP, Hill MA, Davis MJ, Lymphatic vascular integrity is disrupted in type 2 diabetes due to impaired nitric oxide signalling., Cardiovasc. Res 107 (2015) 89–97. 10.1093/cvr/cvv117. [PubMed: 25852084]

[20]. Sellers SL, Iwasaki A, Payne GW, Nitric Oxide and TNFα Are Critical Regulators of Reversible Lymph Node Vascular Remodeling and Adaptive Immune Response, PLoS One. 8 (2013) e60741. 10.1371/journal.pone.0060741.

[21]. Lukacs-Kornek V, Malhotra D, Fletcher AL, Acton SE, Elpek KG, Tayalia P, Collier A, Turley SJ, Regulated release of nitric oxide by nonhematopoietic stroma controls expansion of the

activated T cell pool in lymph nodes, Nat. Immunol 12 (2011) 1096–1104. 10.1038/ni.2112. [PubMed: 21926986]

[22]. Divakaran S, Loscalzo J, The Role of Nitroglycerin and Other Nitrogen Oxides in Cardiovascular Therapeutics, J. Am. Coll. Cardiol 70 (2017) 2393–2410. 10.1016/j.jacc.2017.09.1064. [PubMed: 29096811]

[23]. Sim JY, Nitric oxide and pulmonary hypertension, Korean J. Anesthesiol 58 (2010) 4–14. 10.4097/kjae.2010.58.1.4. [PubMed: 20498805]

[24]. Schudel A, Kassis T, Dixon JB, Thomas SN, S-Nitrosated Polypropylene Sulfide Nanoparticles for Thiol-Dependent Transnitrosation and Toxicity Against Adult Female Filarial Worms, Adv. Healthc. Mater 4 (2015) 1484–1490. 10.1002/adhm.201400841. [PubMed: 25939735]

[25]. Schudel A, Sestito LF, Thomas SN, S-nitrosated poly(propylene sulfide) nanoparticles for enhanced nitric oxide delivery to lymphatic tissues, J. Biomed. Mater. Res. Part A. 106 (2018) 1463–1475. 10.1002/jbm.a.36348.

[26]. Rehor A, Hubbell JA, Tirelli N, Oxidation-Sensitive Polymeric Nanoparticles, Langmuir. 21 (2005) 411–417. 10.1021/la0478043. [PubMed: 15620332]

[27]. Van Der Vlies AJ, O'neil CP, Hasegawa U, Hammond N, Hubbell JA, Synthesis of Pyridyl Disulfide-Functionalized Nanoparticles for Conjugating Thiol-Containing Small Molecules, Peptides, and Proteins, (n.d.). 10.1021/bc9004443.

[28]. Ando T, Jordan P, Joh T, Wang Y, Jennings MH, Houghton J, Alexander JS, Isolation and Characterization of A Novel Mouse Lymphatic Endothelial Cell Line: SV-LEC, Lymphat. Res. Biol 3 (2005) 105–115. 10.1089/lrb.2005.3.105. [PubMed: 16190815]

[29]. Rohner NA, Thomas SN, Flexible Macromolecule versus Rigid Particle Retention in the Injected Skin and Accumulation in Draining Lymph Nodes Are Differentially Influenced by Hydrodynamic Size, ACS Biomater. Sci. Eng 3 (2017) 153–159. 10.1021/acsbiomaterials.6b00438. [PubMed: 29888321]

[30]. Trevaskis NL, Kaminskas LM, Porter CJH, From sewer to saviour — targeting the lymphatic system to promote drug exposure and activity, Nat. Rev. Drug Discov 14 (2015) 781–803. 10.1038/nrd4608. [PubMed: 26471369]

[31]. Roozendaal R, Mempel TR, Pitcher LA, Gonzalez SF, Verschoor A, Mebius RE, von Andrian UH, Carroll MC, Conduits mediate transport of low-molecular-weight antigen to lymph node follicles., Immunity. 30 (2009) 264–76. 10.1016/j.immuni.2008.12.014. [PubMed: 19185517]

[32]. Roozendaal R, Mebius RE, Kraal G, The conduit system of the lymph node, Int. Immunol 20 (2008) 1483–1487. 10.1093/intimm/dxn110. [PubMed: 18824503]

[33]. Gretz JE, Norbury CC, Anderson AO, Proudfoot AE, Shaw S, Lymph-borne chemokines and other low molecular weight molecules reach high endothelial venules via specialized conduits while a functional barrier limits access to the lymphocyte microenvironments in lymph node cortex., J. Exp. Med 192 (2000) 1425–40. http://www.ncbi.nlm.nih.gov/pubmed/11085745 (accessed April 29, 2019). [PubMed: 11085745]

[34]. Randolph GJ, Angeli V, Swartz MA, Dendritic-cell trafficking to lymph nodes through lymphatic vessels, Nat. Rev. Immunol 5 (2005) 617–628. 10.1038/nri1670. [PubMed: 16056255]

[35]. Manolova V, Flace A, Bauer M, Schwarz K, Saudan P, Bachmann MF, Nanoparticles target distinct dendritic cell populations according to their size, Eur. J. Immunol 38 (2008) 1404–1413. 10.1002/eji.200737984. [PubMed: 18389478]

[36]. Heit A, Huster KM, Schmitz F, Schiemann M, Busch DH, Wagner H, CpG-DNA Aided Cross-Priming by Cross-Presenting B Cells, J. Immunol 172 (2004) 1501–1507. 10.4049/jimmunol.172.3.1501. [PubMed: 14734727]

[37]. Schudel A, Chapman AP, Kwan MY, Higgenson CJ, Francis DM, Manspeaker MP, Avecilla ARC, Rohner NA, Finn MG, Thomas SN, Programmable multistage delivery to lymph nodes, Nat. Med 15 (2020) 491–499.

[38]. Kähäri L, Fair-Mäkelä R, Auvinen K, Rantakari P, Jalkanen S, Ivaska J, Salmi M, Transcytosis route mediates rapid delivery of intact antibodies to draining lymph nodes, J. Clin. Invest 129 (2019) 3086–3102. 10.1172/JCI125740. [PubMed: 31232704]

[39]. Triacca V, Guc E, Kilarski WW, Pisano M, Swartz MA, Transcellular Pathways in Lymphatic Endothelial Cells Regulate Changes in Solute Transport by Fluid Stress, Cell. Biol (2017). 10.1161/CIRCRESAHA.116.309828.

[40]. Cromer WE, Zawieja SD, Tharakan B, Childs EW, Newell MK, Zawieja DC, The effects of inflammatory cytokines on lymphatic endothelial barrier function, Angiogenesis. 17 (2014) 395–406. 10.1007/s10456-013-9393-2. [PubMed: 24141404]

[41]. Kang-Decker N, Cao S, Chatterjee S, Yao J, Egan LJ, Semela D, Mukhopadhyay D, Shah V, Nitric oxide promotes endothelial cell survival signaling through S-nitrosylation and activation of dynamin-2., J. Cell Sci 120 (2007) 492–501. 10.1242/jcs.03361. [PubMed: 17251380]

[42]. Saul ME, Thomas PA, Dosen PJ, Isbister GK, O'Leary MA, Whyte IM, McFadden SA, van Helden DF, A pharmacological approach to first aid treatment for snakebite, Nat. Med 17 (2011) 809–811. 10.1038/nm.2382. [PubMed: 21706027]

[43]. Yao S-K, Ober JC, Krishnaswami A, Ferguson JJ,; Vernon Anderson H, Golino P; Maximilian Buja L, Willerson JT, Endogenous Nitric Oxide Protects Against Platelet Aggregation and Cyclic Flow Variations in Stenosed and Endothelium-Injured Arteries, n.d http://ahajournals.org (accessed May 13, 2020).

[44]. Matsushita K, Morrell CN, Cambien B, Yang SX, Yamakuchi M, Bao C, Hara MR, Quick RA, Cao W, O'Rourke B, Lowenstein JM, Pevsner J, Wagner DD, Lowenstein CJ, Nitric oxide regulates exocytosis by S-nitrosylation of N-ethylmaleimide-sensitive factor, Cell. 115 (2003) 139–150. 10.1016/S0092-8674(03)00803-1. [PubMed: 14567912]

[45]. Park JW, Piknova B, Nghiem K, Lozier JN, Schechter AN, Inhibitory effect of nitrite on coagulation processes demonstrated by thrombelastography, Nitric Oxide - Biol. Chem 40 (2014) 45–51. 10.1016/j.niox.2014.05.006.

[46]. Mowbray M, Tan X, Wheatley PS, Morris RE, Weller RB, Topically applied nitric oxide induces T-lymphocyte infiltration in human skin, but minimal inflammation, J. Invest. Dermatol 128 (2008) 352–360. 10.1038/sj.jid.5701096. [PubMed: 17914444]

[47]. Rohner NA, Thomas SN, Woodruff GW, Petit PH, Coulter WH, Flexible Macromolecule versus Rigid Particle Retention in the Injected Skin and Accumulation in Draining Lymph Nodes Are Differentially Influenced by Hydrodynamic Size, (n.d.). 10.1021/acsbiomaterials.6b00438.

[48]. Kang S, Ahn S, Lee J, Kim JY, Choi M, Gujrati V, Kim H, Kim J, Shin EC, Jon S, Effects of gold nanoparticle-based vaccine size on lymph node delivery and cytotoxic T-lymphocyte responses, J. Control. Release 256 (2017) 56–67. 10.1016/j.jconrel.2017.04.024. [PubMed: 28428066]

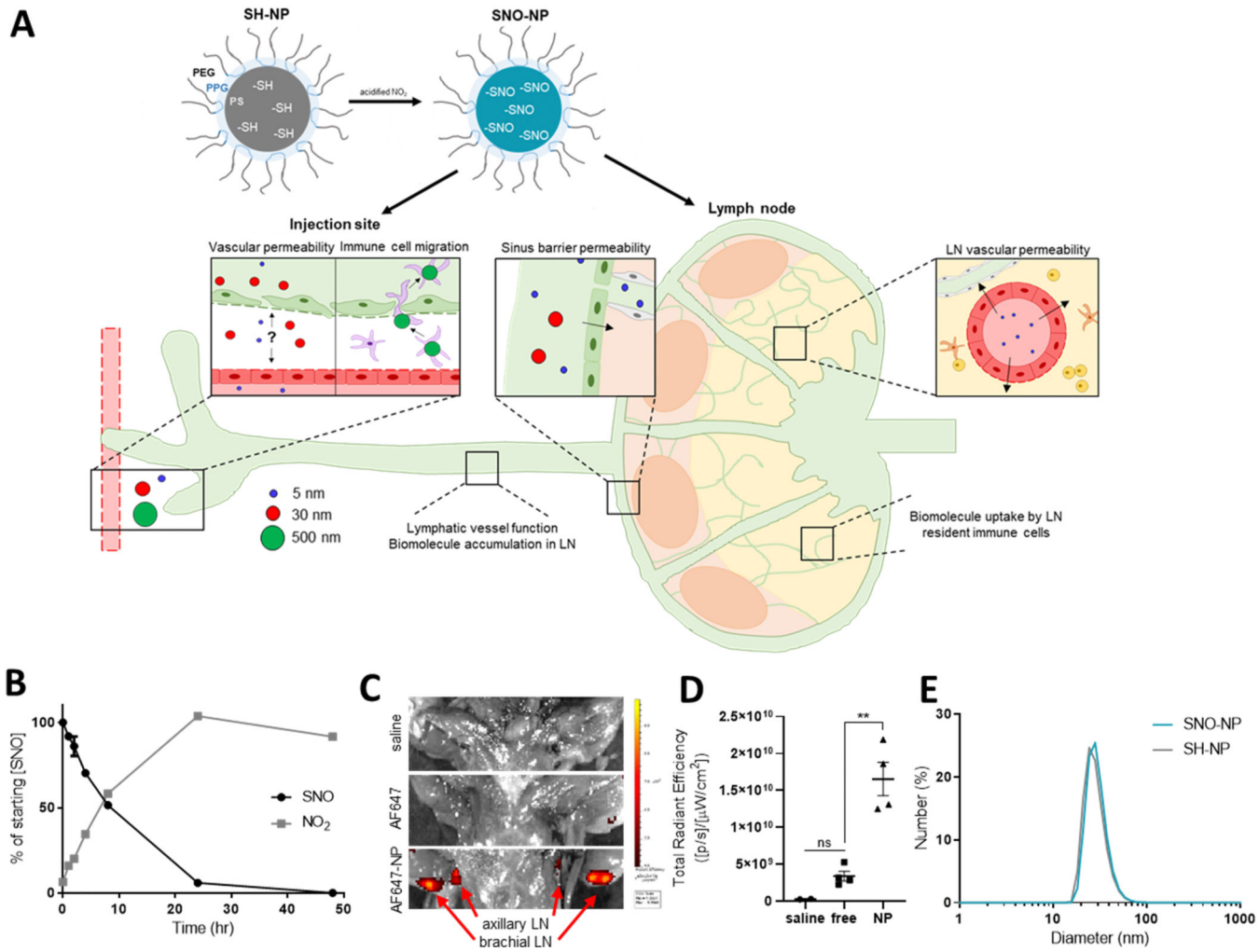

Figure 1. Production and characterization of lymphatic-draining SNO-NP, and potential effects of delivered NO.

A) Schematic of NP nitrosation and potential NO effects after peripheral administration. Thiolated SH-NP can be loaded with NO by reaction with acidified nitrite, forming SNO-NP that enable NO delivery to the lymphatics. NO delivered by SNO-NP is a pleiotropic molecule that can have a variety of effects on biomolecule transport, including local effects at the site of injection, modulation of lymphatic drainage, and altered lymph node (LN) permeability or immune cell activation. B) S-nitrosothiol (SNO) and nitrite (NO2) concentration in a solution of SNO-NP over time. C) IVIS imaging of AF647-labeled NP draining to axillary and brachial LN from a forelimb injection, and D) quantification of C. E) Diameter of SNO-NP and SH-NP as measured by dynamic light scattering.

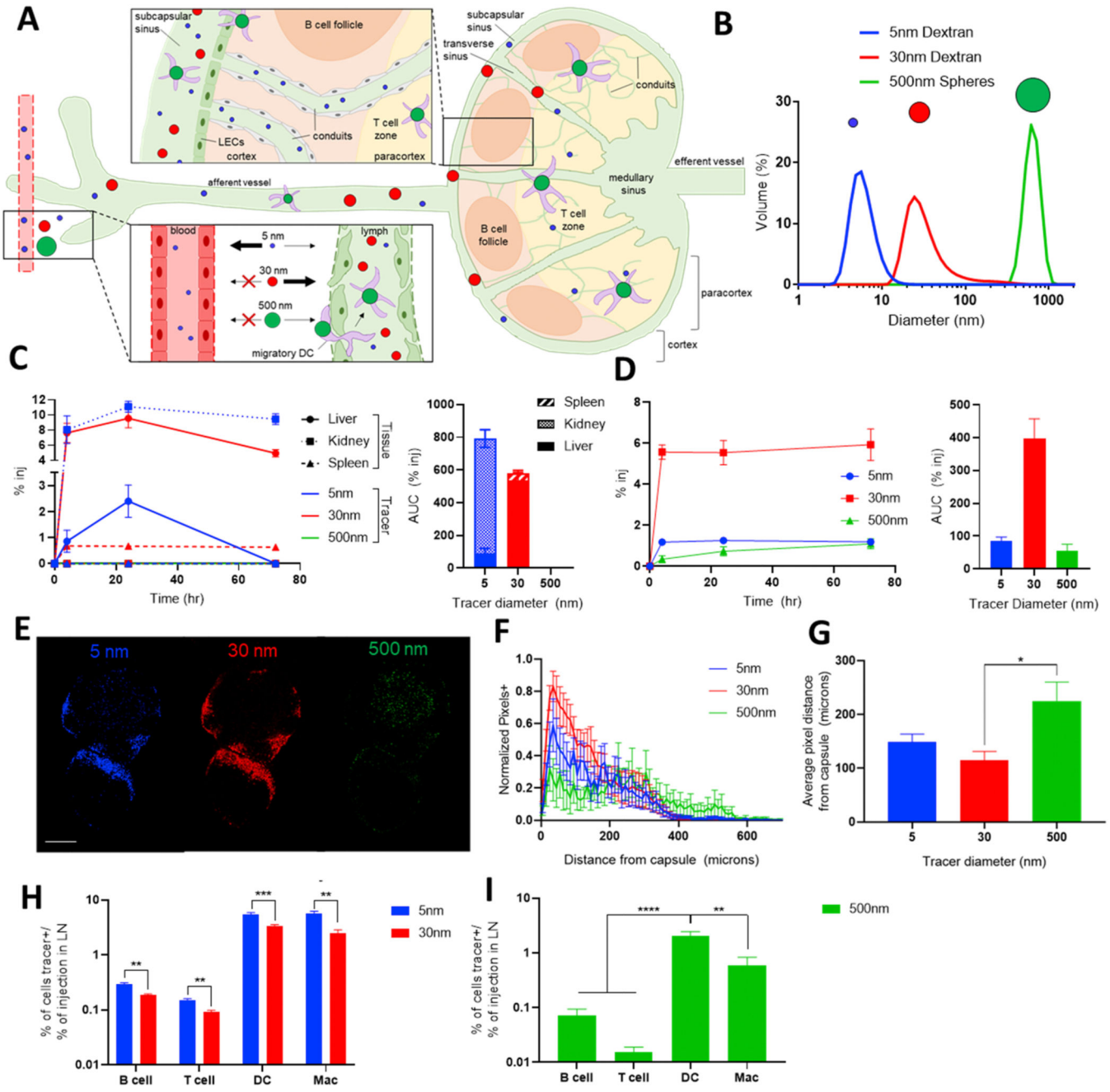

Figure 2. Lymphatic transport is regulated by molecule size, and a tracer panel can probe this differential transport.

A) Schematic of size-based effects on molecule drainage from the interstitium and into draining LNs (dLNs). Blue = 5 nm, red = 30 nm, and green = 500 nm molecules. B) Diameter of selected fluorescent tracers as measured by dynamic light scattering. C) Time course of tracer biodistribution in systemic organs based on their size (left), and their total accumulation in each organ (right). Tracers are cleared from systemic circulation according to their size, with 5 nm clearance in the kidney and 30 nm clearance by the liver. D) Timecourse of tracer appearance in the dLN based on their size (left) and total accumulation,

measured by area under the curve (right). 30 nm tracers reach the LN more efficiently than 5 or 500 nm tracers. Passively draining tracers show significant signal in the dLN within 4 h, while 500 nm tracers show a more gradual appearance in the dLN. E) Confocal microscopy images of tracer distribution within a brachial LN 72 h after ipsilateral forelimb injection. Scale bar = 500 μm. F) Quantified distribution of tracer+ pixels in axillary and brachial LN draining forelimb injections. 30 nm tracers show a more peripheral bias than lower accumulating 5 nm tracer. Beyond 400 μm from the LN capsule, 500 nm signal is greater than that of passively draining tracers. G) Average tracer penetration depth. H) 5 nm tracers have improved access to LN cells compared to larger 30 nm tracers. I) Actively transported 500 nm tracers tend to appear preferentially in DCs. In G and I, broad cell types are defined as follows: B cell (B220+CD3-CD11b-), T cell (CD3+B220-), DC (CD11c+), macrophage (F4/80+).

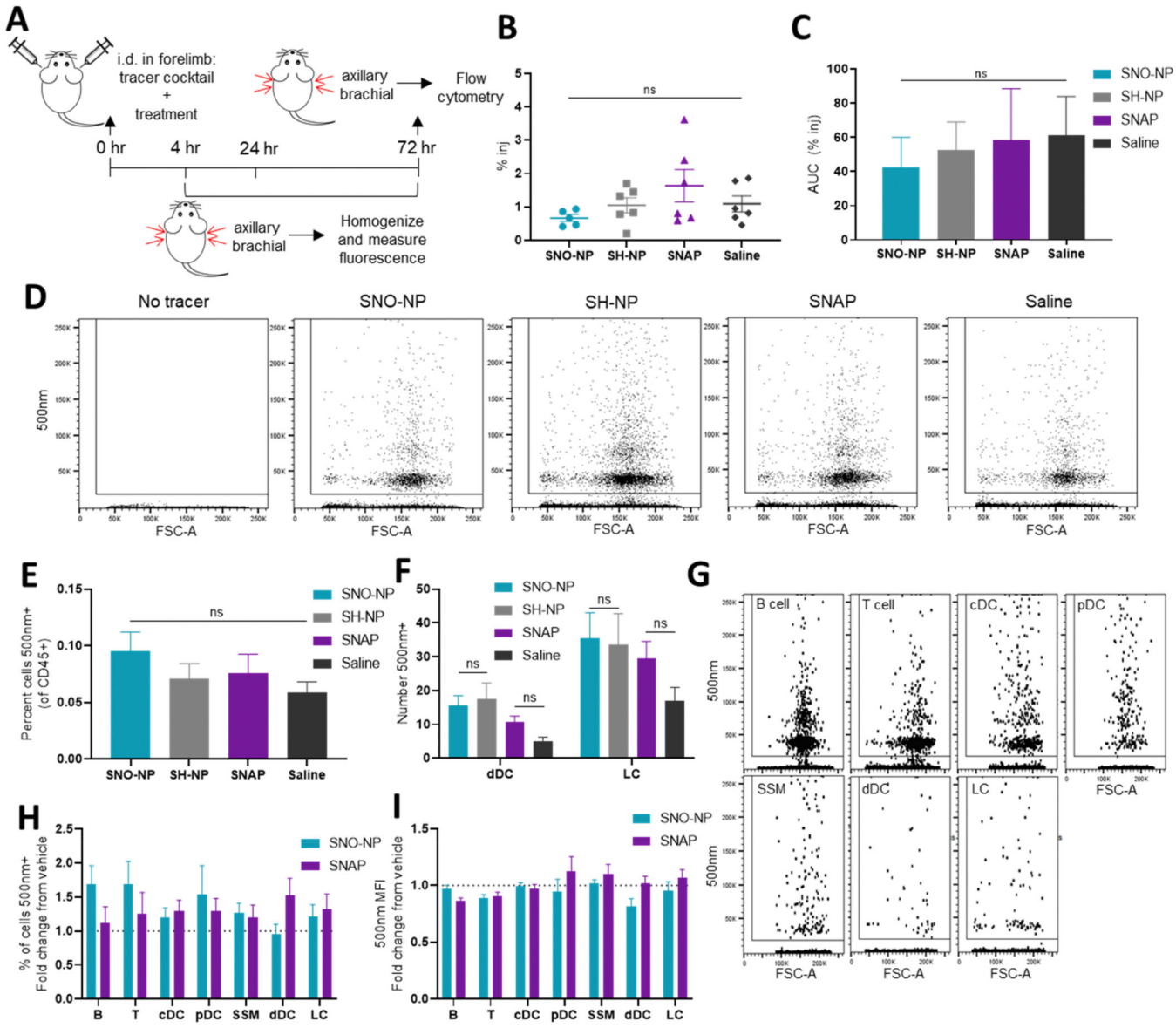

Figure 3. Active transport of microparticles from injection site is unaltered by SNO-NP co-injection.

A) Experimental schematic in tracer distribution studies. B) Percent of injection of 500 nm tracer in the dLN 72 h after injection. C) Total exposure (AUC) of dLN to 500 nm tracer over the course of 72 h. D) 500 nm tracer uptake by LN cells is detectable by flow cytometry. E) The percent of CD45+ cells within the dLN that are 500 nm tracer+ with SNO-NP or control treatment. F) The number of 500 nm+ dDCs and LCs found in LNs draining a tracer injection. G) Representative dot plots of 500 nm+ LN cells. H) Percent of cells 500 nm+ in dLN. I) Mean fluorescence intensity of 500 nm+ cell populations in the dLN.

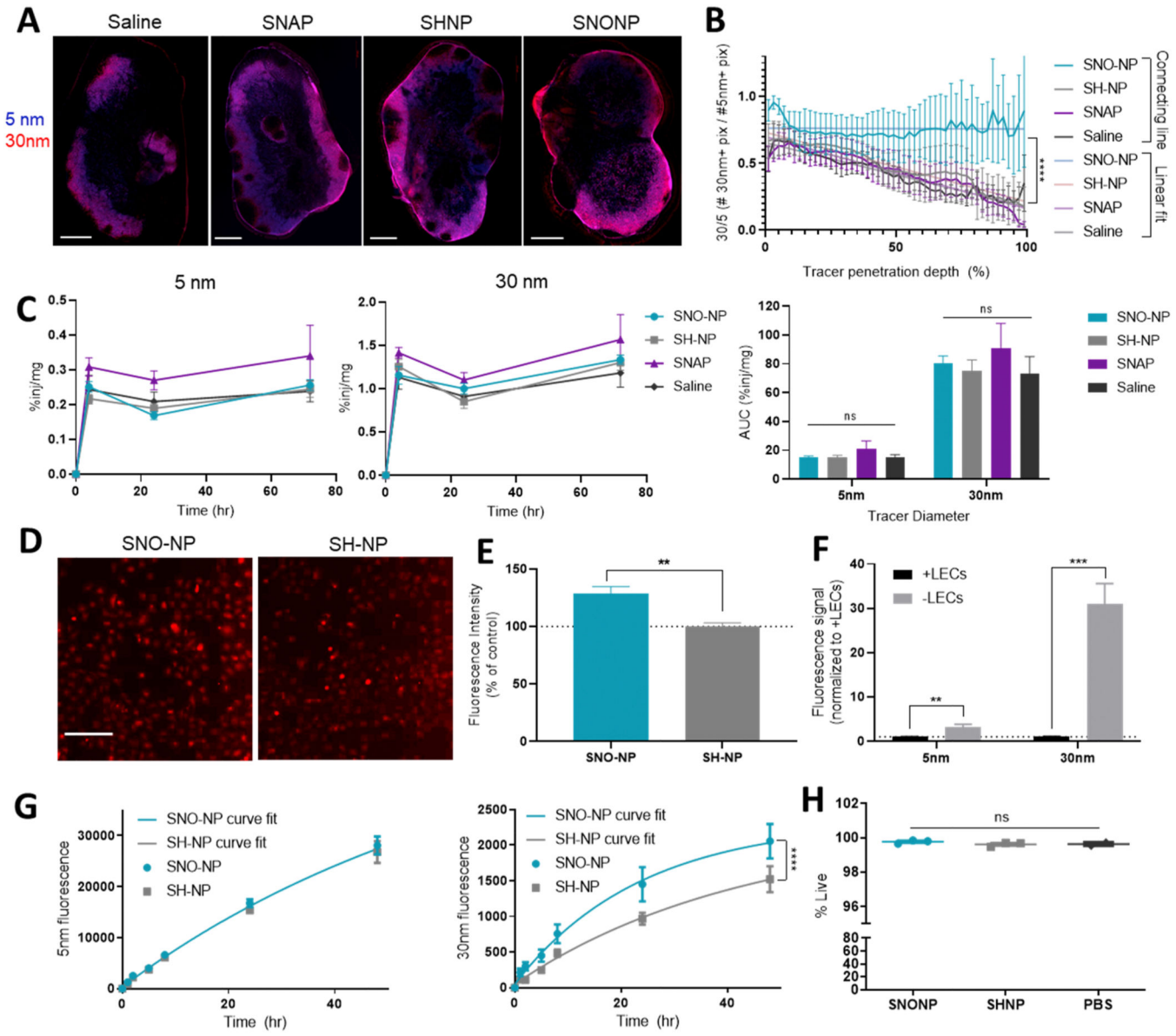

Figure 4. LN-targeted NO delivery by SNO-NP, but not by SNAP, increases penetration of passively draining 30 nm tracer into the dLN.

A) 5 nm (blue) and 30 nm (red) tracer distribution in the LN 72 h after co-injection with treatment. Scale bar = 500 μm. B) Quantification of tracer distribution in the LN. **** indicates significant difference ($p<0.0001$) between SNO-NP linear fit and other treatments. C) Percent of injection in dLN over time for 5 nm (left) and 30 nm (center), and their AUC. D) 30 nm tracer (red) uptake by SV-LECs in in vitro culture after 4 h. Scale bar = 200 μm. E) Fluorescence intensity of SV-LECs incubated with 30 nm dextran and treatments. F) Fluorescence of 5 nm or 30 nm tracers that pass through a transwell membrane with or without an SV-LEC monolayer after 48 h. G) Fluorescence of 5 nm dextran (left) or 30 nm dextran (right) that penetrates an SV-LEC monolayer over time. Lines represent nonlinear fits. H) Viability of SV-LECs after 48 h of incubation with tracer and SNO-NP or controls.

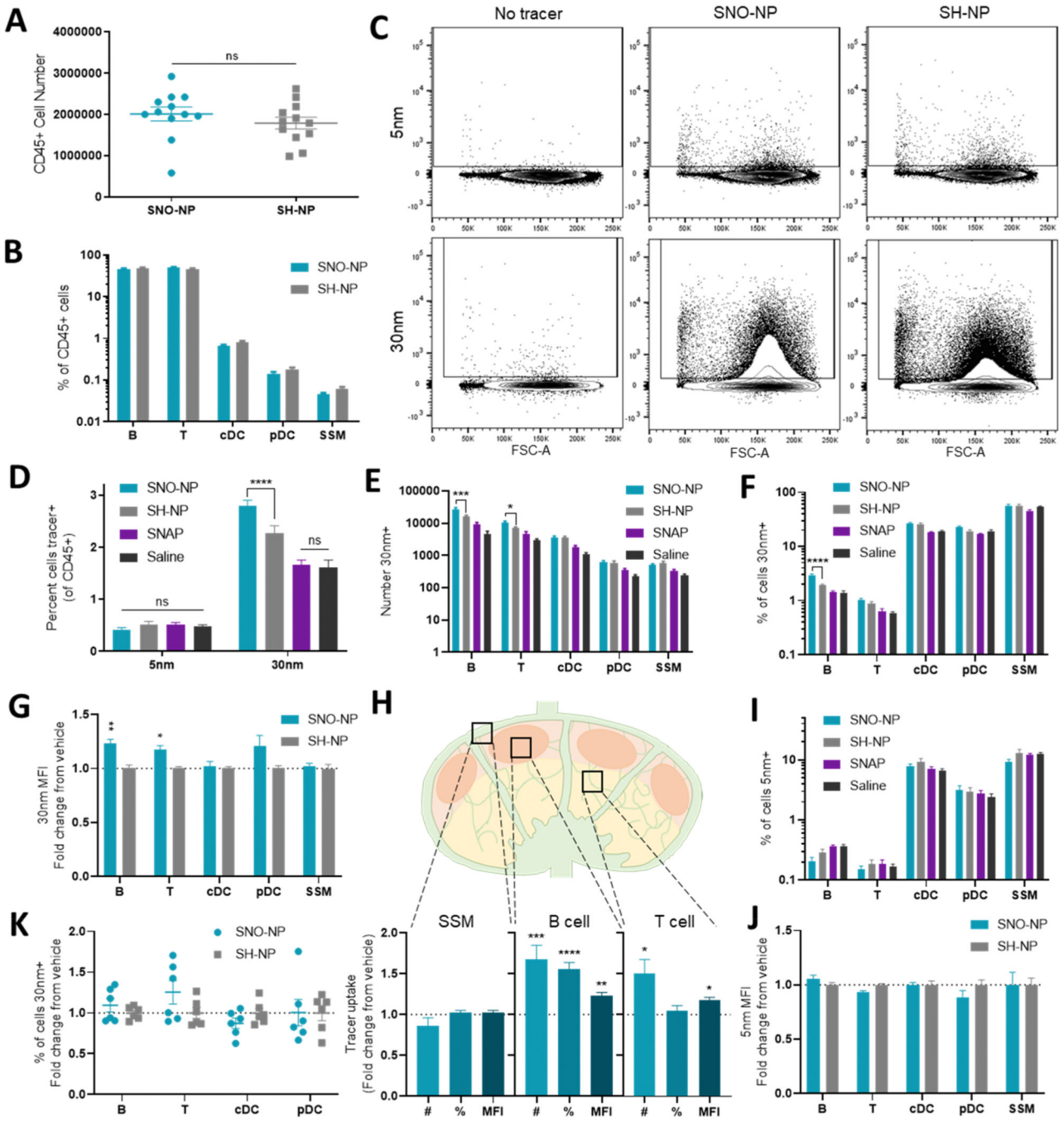

Figure 5. SNO-NP treatment increases the uptake of passively drained 30 nm tracer by LN cells in vivo, but not of smaller 5 nm tracers.

A) CD45+ cell number in dLN. B) The cellular profile of CD45+ LN cells with SNO-NP treatment and control SH-NP treatment. C) Representative examples of CD45+ LN cells without 5 and 30 nm tracers, or with tracer and SNO-NP or SH-NP treatment. D) Percent of CD45+ cells in dLN positive for passively draining tracers 72 h after co-injection with treatment. E) Number and F) percent of each cell subtype positive for 30 nm tracer after 72 h. G) MFI of 30 nm+ cells after SNO-NP treatment, normalized to SH-NP control. *s represent significant differences between pre-normalized populations. H) Effect of SNO-NP

treatment on tracer uptake by barrier, cortex, and paracortex cell populations. I) Percent of LN cells positive for 5 nm tracer 72 h after injection. J) Mean fluorescence intensity of 5 nm + cells 72 h after tracer and SNO-NP injection, normalized to SH-NP control. K) Percent of cells positive for 30 nm tracer after splenocytes were incubated in vitro for 4 h with tracer and SNO-NP or SH-NP control. Results are normalized to SH-NP control.

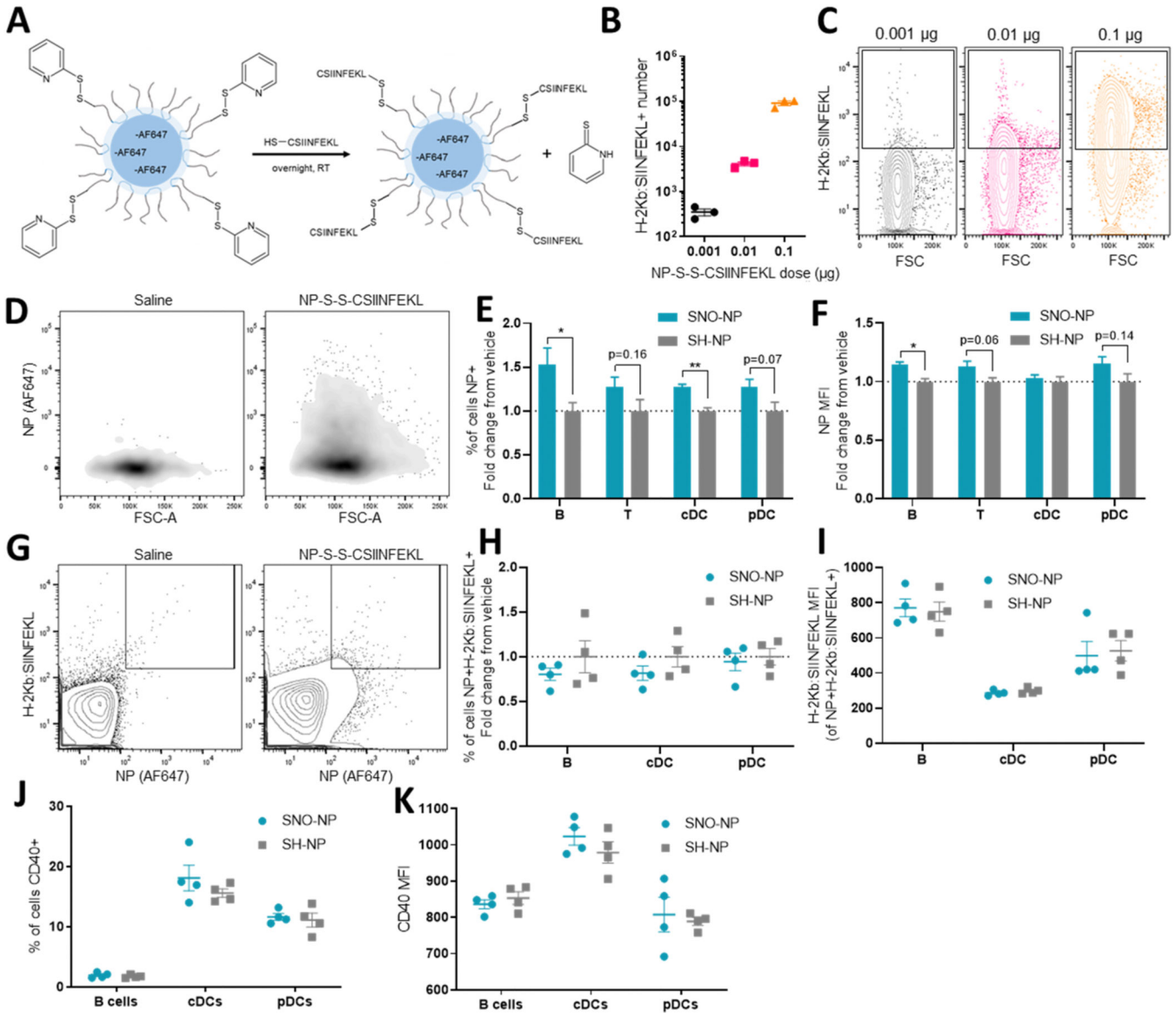

Figure 6. SNO-NP treatment increases uptake of peptide-conjugated NP-S-S-CSIINFEKL by LN cells but does not affect antigen cross-presentation or cell activation.

A) Schematic of NP-S-S-CSIINFEKL synthesis. Alexa Fluor 647-labeled, PDS-functionalized NP are incubated with thiolated CSIINFEKL peptide overnight at room temperature, resulting in the formation of NP-S-S-CSIINFEKL. B) CSIINFEKL presentation by CD45+ splenocytes increases with increasing NP-S-S-CSIINFEKL dose after 18 h of incubation in vitro, as evidenced by increasing H-2KB:SIINFEKL+ cell counts and C) increasing fluorescent intensity in H-2KB:SIINFEKL+ cells. D) Representative density plots of CD45+ LN cells with (right) and without (left) injection of 647-labeled NP-S-S-CSIINFEKL. E) Percent of cells that are positive for NP-S-S-CSIINFEKL 72 h after co-injection of NP-S-S-CSIINFEKL and treatment. F) AF647 MFI of NP+ cells. G) Representative contour plots of CSIINFEKL-presenting, NP+ CD45+ cells in LN receiving a saline (left) or NP-S-S-CSIINFEKL (right) injection. H) Percent of cells that are both NP+

and presenting CSIINFEKL, normalized to SH-NP control. I) CSIINFEKL MFI in double positive cells. J) Percent of cells expressing CD40 and K) the MFI of CD40+ cells.